J. Fluid Mech. (1989), *vol.* 208, *pp.* 479–507
Printed in Great Britain

Upper bounds on functions of the dissipation rate in turbulent shear flow

By W. V. R. MALKUS AND L. M. SMITH
Massachusetts Institute of Technology, Department of Mathematics, Cambridge, MA 02139, USA

(Received 23 June 1988 and in revised form 27 April 1989)

The search for a statistical stability criterion characterizing steady-state turbulent shear flows has led us to the study of a function proportional to the ratio of the fluctuation dissipation rate and the dissipation rate of the mean. The first Euler–Lagrange equations for an upper bound of this function have optimal solutions with the observed scaling laws and an asymptotic velocity defect for turbulent channel flow. As in the case of maximum transport, the optimal solution for the model equations is a discrete spectrum of streamwise vortices. It is shown how these solutions can be brought closer to the realized flow with additional constraints on the smallest vortex.

1. Introduction

The central purpose of this study is to seek functions whose upper bounds scale correctly and lie close enough to observed means that the optimizing vector fields reflect the principal physics of the realized fluid motions. Past work on the upper-bound approach to turbulent flow has been restricted to the search for limits on the transport of heat, mass or momentum. Here, analytic and numerical procedures are developed to explore bounds on any moment or product of moments of the mean flow.

The development of formal upper-bound theory is due to Howard (1963) in his study of the heat transported by turbulent convection. The approach taken is to seek an extreme of some averaged flow property from a set of vector fields satisfying boundary conditions, continuity conditions and conditions imposed by 'energy' integrals of the complete equations describing the flow. Since the realized solutions are contained in the set of fields considered, the deduced extreme will be a quantitative bound on actual measurements. In principle this bound can be brought closer and closer to the observed value by imposing additional derived constraints. The vector fields found as solutions of the Euler–Lagrange equations for these extremes represent a complete mechanistic idealization, determining not only the bound which has been sought, but all statistical properties of the model flow. If the flow property studied has an extreme close to the observations for all Reynolds numbers, then it is likely that many other statistical properties of the optimizing vector fields will also be adjacent to the realized flow.

Upper-bound theory can be thought of as an 'opener', since more vector fields are admitted for consideration than those which are solutions of the Navier–Stokes equations. The theory emphasizes the order in turbulent flow, not the disorder. However, order and disorder appear to play roughly equal roles in most flows. Many other studies of turbulent statistics are based on 'closures', which are plausible

truncations of deduced relations between statistical properties of the flow. Many closures emphasize the disordered aspects of turbulence. Recent work using a modification of Kraichnan's (1959) 'direct-interaction approximation' closure in an application to shear flow (Yakhot & Orszag 1986) will be discussed in the conclusion.

The plan of this paper is to present certain analytically accessible bounds on mean flow properties in the following section. The work of Howard (1972) is briefly reviewed and extended to dissipation rate functions suggested by recent studies of statistical stability (Ierley & Malkus 1988).

A third section describes the multiscale structure of the optimum solutions first found by Busse (1969). That work permits the determination of a critical boundary Reynolds number associated with the Busse–Howard smallest scale of motion. Utilizing this smallest scale, a simplified upper-bound problem is outlined, which relaxes the viscous constraints on all but the boundary scale of motion and focuses on the stability of the mean flow.

In §4, the Euler–Lagrange equations for maximum momentum transport in the simplified upper-bound problem are formulated, solved numerically, and as anticipated shown to be even less constrained than the earlier Busse (1978) results.

Section 5 describes numerical and analytic results for bounds on other functions of the dissipation rate integral.

In §6, solutions are found for extreme properties of a unique integral, discovered during this work and defined here as the efficiency function. Its asymptotic velocity defect and logarithmic region have the scaling found in experiments. The quantitative error appears to be attributable to insufficient constraint in determining the critical Reynolds number of the smallest scale.

Section 7 introduces additional constraints, but only for the smallest scale. A first use of these constraints leads to a cross-stream vortex wave as the preferred mode. A second step explores numerically the stability boundary of vortex waves to three-dimensional inertial instabilities (Bayly, Orszag & Herbert 1988). The resulting critical Reynolds number for the boundary is an order of magnitude larger than the Busse–Howard value. In consequence the quantitative upper-bound prediction for the mean field for turbulent Poiseuille flow is within 25% of the observations at all Reynolds numbers above 5000.

In the concluding §8 possible formal links between the ordered vector fields of upper-bound theory and disordered fields of dynamic system and closure theories are explored. It is proposed that the upper-bound fields be treated as zeroth-order mean fields, upon which dynamical or statistical perturbative methods can lead to intermittency and decorrelation. Finally the generalizability of the efficiency-function bound is questioned. Its formal relation to the statistical stability of shearing flow has yet to be established.

2. Bounds on properties of the mean flow

2.1. *The search for a statistical stability criterion*

Nonlinear perturbation theory near points of instability leads to the conclusion that, with occasional hysteresis, solution degeneracy is removed in favour of the solution of maximum transport. Both for this and for pragmatic reasons the only bound on fully turbulent flow that has been explored in past literature is that of extreme transport. However, many other integral properties of the flow related to transport are also maximum in the small-amplitude limit where this stability criterion is correct. Here, in a broadened search for an asymptotic statistical stability criterion,

we investigate classes of mean field moments which correspond to maximum transport at the point of instability, but can have quite different parametric behaviour at large Reynolds numbers.

In Ierley & Malkus (1988) the stability conditions for two-dimensional and three-dimensional disturbances were assessed by largely numerical methods for a model turbulent shear flow. Two observations in that work relevant to this paper were that an 'energy' method led to a critical value for a boundary Reynolds number close to the observed value; and that an extreme of the ratio of fluctuation and mean dissipation rates was also close to that of the observed flow. Both of those findings provide guidance in the following.

2.2. *Formal bound theory*

Howard's work on upper bounds did not direct attention to statistical stability. Stress was placed on the formal correctness of the bound itself. Howard's approach will be generalized in this section for an exploration of the parameter dependence of bounds on a variety of mean field moments. This approach provides an overview which will be exploited in following sections. For simplicity of description, the plane Couette flow case, treated in Howard's (1972) review article, is studied in this first section. The incompressible Navier–Stokes equations are written

$$\frac{\partial \boldsymbol{v}}{\partial t}+\boldsymbol{v}\cdot\boldsymbol{\nabla v}+\boldsymbol{\nabla} P = R^{-1}\nabla^2\boldsymbol{v}, \quad \boldsymbol{\nabla}\cdot\boldsymbol{v}=0, \tag{2.1}$$

where the Reynolds number R is based on the boundary velocity and on the half-interval, with boundary conditions $\boldsymbol{v} = \mp\hat{\boldsymbol{\imath}}$ on $z = \pm 1$. For statistically steady flow, an average over a plane at constant z of (2.1) leads to

$$\overline{uw}+R^{-1}\beta = \tau_0, \tag{2.2}$$

where τ_0 is the constant stress per unit mass, the overbar represents the average over a plane, $\overline{uw}$ is the Reynolds stress and $\beta \equiv (-\partial\bar{v}\cdot\hat{\boldsymbol{\imath}})/\partial z$ is the negative mean velocity gradient. A bracket $\langle\ \rangle$ will indicate an average over the entire flow, here $\langle\beta\rangle = 1$. Equation (2.2), the boundary conditions, and the fluctuation 'energy' integral are the only constraints used to determine a first upper bound on the turbulent momentum transport. This integral is found by multiplying (2.1) by $\boldsymbol{u} = \boldsymbol{v}-\bar{\boldsymbol{v}}$ and integrating over the fluid. Hence, in the statistically steady state,

$$\langle\overline{uw}\beta\rangle = R^{-1}\langle|\boldsymbol{\nabla u}|^2\rangle, \tag{2.3}$$

properly called the fluctuation dissipation rate integral. Then using (2.2) Howard eliminates β from (2.3) and writes

$$\langle\overline{uw}\rangle - R\langle(\overline{uw}-\langle uw\rangle)^2\rangle = R^{-1}\langle|\boldsymbol{\nabla u}|^2\rangle. \tag{2.4}$$

However, the total energy dissipation rate is proportional to

$$F \equiv \tau_0 R = \langle|\boldsymbol{\nabla v}|^2\rangle = \langle|\boldsymbol{\nabla u}|^2\rangle+\langle\beta^2\rangle. \tag{2.5}$$

Hence

$$F = 1+R^2\langle(\overline{uw}-\langle uw\rangle)^2\rangle+\langle|\boldsymbol{\nabla u}|^2\rangle = 1+R\langle\overline{uw}\rangle \tag{2.6}$$

and from these equations Howard constructs the homogeneous functional

$$F = 1+\frac{\langle\overline{uw}\rangle^2-R^{-1}\langle|\boldsymbol{\nabla u}|^2\rangle\langle\overline{uw}\rangle}{\langle(\overline{uw}-\langle uw\rangle)^2\rangle}. \tag{2.7}$$

An upper bound on F determines a maximum stress as a function of R.

To find an estimate from above this extreme, Howard proved that, with the constraint of boundary conditions,

$$\frac{\langle(\overline{uw}-\langle\overline{uw}\rangle)^2\rangle}{\langle\overline{uw}\rangle^2} \geqslant \frac{\langle\overline{uw}\rangle}{3\langle|\nabla \boldsymbol{u}|^2\rangle}. \tag{2.8}$$

Then, from (2.7) and (2.8) he concludes that

$$1 \leqslant F \leqslant 1+\tfrac{3}{4}R. \tag{2.9}$$

The observed value of F is much smaller, yet the observed asymptotic dependence of F on R differs only by the logarithm of R.

2.3. *Other bounds; the H function*

To generalize Howard's work to other moments of the mean flow requires a method for the construction of homogeneous functionals for these other moments. A dissection of Howard's approach suggests rewriting (2.4) as

$$1 = \frac{R\langle(\overline{uw}-\langle uw\rangle)^2\rangle}{\langle\overline{uw}\rangle - R^{-1}\langle|\nabla \boldsymbol{u}|^2\rangle} \equiv H, \tag{2.10}$$

where H is an inhomogeneous identity, of order two in the fluctuating velocities. Then any moment can be written in homogeneous form using H. For example, Howard's functional for momentum transport emerges if one writes

$$R\langle\overline{uw}\rangle = R\langle\overline{uw}\rangle H^{-1} = \frac{\langle\overline{uw}\rangle(\langle\overline{uw}\rangle - R^{-1}\langle|\nabla \boldsymbol{u}|^2\rangle)}{\langle(\overline{uw}-\langle\overline{uw}\rangle)^2\rangle}. \tag{2.11}$$

For a moment of mixed order, such as $\langle\beta\overline{uw}\rangle$, one writes

$$\begin{aligned}\langle\beta\overline{uw}\rangle &= \langle\overline{uw}\rangle H^{-1} - R\langle(\overline{uw}-\langle\overline{uw}\rangle)^2\rangle H^{-2} \\ &= \frac{R^{-2}\langle|\nabla \boldsymbol{u}|^2\rangle(\langle\overline{uw}\rangle - R^{-1}\langle|\nabla \boldsymbol{u}|^2\rangle)}{\langle(\overline{uw}-\langle\overline{uw}\rangle)^2\rangle}.\end{aligned} \tag{2.12}$$

Similarly, one finds that

$$\frac{R\langle\beta\overline{uw}\rangle}{\langle\beta^2\rangle} = \frac{R^{-1}\langle|\nabla \boldsymbol{u}|^2\rangle(\langle\overline{uw}\rangle - R^{-1}\langle|\nabla \boldsymbol{u}|^2\rangle)}{\langle(\overline{uw}-\langle\overline{uw}\rangle)^2\rangle + (\langle\overline{uw}\rangle - R^{-1}\langle|\nabla \boldsymbol{u}|^2\rangle)^2}. \tag{2.13}$$

A principal virtue of the homogeneous form is the freedom from an amplitude constraint and the consequent simplification of the functional one seeks to optimize. For example, one may define

$$f(z) = \frac{\overline{uw}}{\langle\overline{uw}\rangle}, \quad \eta \equiv \frac{R^{-1}\langle|\nabla \boldsymbol{u}|^2\rangle}{\langle\overline{uw}\rangle};$$

then (2.13) is written

$$\frac{R\langle\beta\overline{uw}\rangle}{\langle\beta^2\rangle} = \frac{\eta(1-\eta)}{\langle(1-f(z))^2\rangle + (1-\eta)^2} \equiv I. \tag{2.14}$$

Using Howard's estimate from above, (2.8), rewritten as

$$\langle(1-f(z))^2\rangle \geqslant \tfrac{1}{3}R\eta,$$

one finds an upper bound at high R for the ratio of fluctuating and mean dissipation rates, I in (2.14), to be less than $(\sqrt{3}/2)R^{\frac{1}{2}}$. In realized flows, I increases only as $\ln R$. Hence I alone is a poor candidate in this search.

More relevant examples are upper bounds on $\tau_0^n I$, where n is any number. This function reflects both the low-amplitude preference for maximum τ_0 and the numerical suggestion that I has a local maximum near the observed flow. From (2.5), (2.8), (2.11) and (2.14) one sees that

$$\tau_0^n I \leqslant \left[\frac{1}{R}\frac{(1-\eta)}{(\frac{1}{3}R\eta)}\right]^n \left(\frac{\eta(1-\eta)}{(\frac{1}{3}R\eta)+(1-\eta)^2}\right). \tag{2.15}$$

Although determining the numerical coefficients for maximum $\tau_0^n I(\eta)$ requires tedious computation, it is easily established that the maximum varies as $R^{\frac{1}{2}(1-n)}$ for $n < 1$, and varies as R^0 for $n > 1$. Hence, among the functions of (2.15), $\tau_0 I$ is that special function whose maximum is marginally influenced by the dissipation rate ratio, I. The implications of this rough parametric bound will be quantitatively assessed in §6.

Additional constraints on the class of vector fields permitted in the optimization can improve these bounds. Yet, it has been found that the constraint of continuity does not alter the asymptotic dependence on Reynolds number. The rich structure of optimizing solutions resulting from the constraint of continuity are discussed in the following section.

3. The smallest scale of motion

3.1. *Euler–Lagrange equations for Poiseuille channel flow*

The first integral of the equations of motion for Poiseuille flow may be written

$$\overline{uw} + R_\tau^{-1}\beta = z, \tag{3.1}$$

$$U_\tau^2 \equiv \tau_0, \quad R_\tau \equiv z_0 U_\tau/\nu, \quad \langle \beta z \rangle = RR_\tau^{-1},$$

where, as in the Couette case, the boundaries of the channel are chosen to be $z = \pm 1$, and τ_0 is the magnitude of the stress at the boundary. However, the Reynolds number R is defined using the mean velocity and the half-interval. Here, and in all sections to follow, velocity components are scaled with the 'friction velocity', U_τ. In the customary notation, the mean velocity so scaled is written $U^+(z)$.

The total dissipation rate, from (3.1), is proportional to

$$RR_\tau^2 = R_\tau^3 \langle \beta \overline{uw} \rangle + R_\tau^2 \langle \beta^2 \rangle. \tag{3.2}$$

Also, from (3.1), $$\langle z\overline{uw} \rangle + RR_\tau^{-2} = \tfrac{1}{3}, \tag{3.3}$$

while $$\frac{\tau_0}{(\tau_0)_{\text{laminar}}} = 1 + \frac{R_\tau^2}{R}\langle z\overline{uw} \rangle = \frac{1}{3}\frac{R_\tau^2}{R} \equiv N, \tag{3.4}$$

is defined as the momentum transport Nusselt number. It was this quantity which was maximized, for R fixed, in previous upper-bound studies of Poiseuille flow.

Variational optimization of (3.4), subject to the constraint of the fluctuation dissipation rate integral, to the condition that $\boldsymbol{v} = 0$ on the boundaries and that

$\nabla \cdot \boldsymbol{v} = 0$, leads to the following Euler–Lagrange equations for the components u, v, w of $\boldsymbol{v}$ and an effective pressure ϕ:

$$\left.\begin{aligned} u[az + b\overline{uw}] &= -\frac{\partial \phi}{\partial z} + \nabla^2 w, \\ 0 &= -\frac{\partial \phi}{\partial y} + \nabla^2 v, \\ w[az + b\overline{uw}] &= -\frac{\partial \phi}{\partial x} + \nabla^2 u, \\ \nabla \cdot \boldsymbol{v} &= 0, \end{aligned}\right\} \tag{3.5}$$

where a and b are (constant) functions of integrals of the motion and of R. All functions of the mean flow, whose qualitative bounds were discussed in §1, have Euler–Lagrange equations identical in form to (3.5), differing only in the explicit integrals which enter into a and b.

A first observation concerning (3.5) is that it is separable in the (x, y)-plane, for the nonlinear term $\overline{uw}$ is a function of z only.

Busse's (1969) fascinating addition to Howard's (1963) paper was the discovery that the optimizing solution consisted of many downstream vortices of increasing wavenumber α_n, up to some maximum $\alpha_m(R)$. Smaller-scale vortices are nested inside the next larger vortex, the very smallest vortex defining a boundary layer for the optimum flow. Utilizing Howard's earlier calculation, Busse determined that the effective boundary-layer thickness was $z^+ = 6.30$, where the customary boundary coordinate $z^+ \equiv (1+z)R_\tau$ is used near the $z = -1$ boundary. This thickness is smaller than the observed value by a factor of three, presumably because the optimum vector field is a more efficient transporter of momentum than the realized turbulent flow. However, Busse showed that there was good qualitative agreement between the spatial variation of the r.m.s. values of the fluctuating optimum field and observations near the boundary.

Far from the boundary, both qualitative and quantitative features of the N upper-bound solution fail to agree with observation. The optimum solution has no logarithmic region and no velocity defect 'law' at all. It will be found that solutions for upper bounds other than N do have internal features, but only those of $\tau_0 I$, of (2.15), appears to scale as do the observations.

Busse found the upper bounds for N analytically, but with a boundary-layer approach in which he wrote of the need for computational assistance to resolve aspects of the problem. Upper-bound solutions for the functions of §2.3 will have similar nested vortex solutions, and even more difficult integral constraints. Hence, to make possible a first exploration of a number of other extreme fields, a simplified problem is sought, bounding these bounds from above. Having discovered a property of the flow, whose bound exhibits observed scaling and observed qualitative features, one can return to the complete dynamic model given by the appropriate Euler–Lagrange equations.

3.2. *A less constrained upper-bound problem*

The approach taken here is to study first the extreme structure of the mean field alone. This is implemented in two steps. First an additional local stability constraint compatible with Busse's extreme solution is imposed on the mean flow. Secondly, the dissipation rate integral constraint is applied only to the smallest scale of motion, all

larger scales being free (inviscid) to reach an optimum amplitude. Hence, a determination of maximum transport in this simplified problem will bound Busse's results from above.

The local stability constraint for inviscid parallel flow of one sign is the Rayleigh criterion that the curvature of the flow be everywhere of the same sign. Arnol'd (1965) has extended Rayleigh's results to include finite-amplitude two-dimensional as well as infinitesimal disturbances. Hence the Arnol'd–Rayleigh condition should be met by the finite-amplitude two-dimensional extreme solutions of the Euler–Lagrange equations (3.5). Both the observations and Busse's optimal N solutions exhibit no inflexions in the mean flow. However, the dissipation rate integral does not capture the physics of the Rayleigh criterion, which has its origin in vorticity constraints. Hence, the inflexional constraint should be retained in the determination of optimal solutions of the Euler–Lagrange equations (3.5) for functions other than N. The occurrence of local travelling inflexions is discussed in §7, where vorticity constraints on the smallest scale of motion are considered.

The formal upper-bound problem to be addressed in the following three sections is as follows:

(*a*) A critical boundary Reynolds number for a smallest scale of motion, k_0 is determined by the dissipation rate integral. As a first estimate, the Busse–Howard determination of a boundary Reynolds number for stability is used. A new determination is made in §7.

(*b*) The curvature of the mean flow is required to remain of one sign by using the Fejér representation

$$-\frac{\partial^2 U^+}{\partial z^2} = I^* I, \quad I \equiv \sum_0^{k_0} I_k \, e^{ik\phi}, \tag{3.6}$$

where $\phi \equiv (1+z)\,\pi$, and I^* indicates the complex conjugate.

(*c*) The constraints imposed on the I_k by the boundary conditions $\boldsymbol{v} = 0$, and continuity conditions $\boldsymbol{\nabla} \cdot \boldsymbol{v} = 0$ are determined.

(*d*) Subject to these constraints, various functionals (e.g N, $\langle \beta \overline{wu} \rangle$ I) are optimized and the resulting mean fields are determined and exhibited.

Numerical methods are particularly straightforward and complete for values of $k_0 < 10^2$. Asymptotic analytic methods are checked with numerical methods for $10^2 < k_0 < 10^3$, and used for higher k_0.

4. The Euler–Lagrange equations and mean flow for maximum Nusselt number

4.1. *The conditions on I_k and k_0*

Within the context of the problem posed at the end of §3, an upper bound is sought for the Nusselt number as a function of the Reynolds number. It was shown in §2.2 that the bound of maximum Nusselt number is equivalent to both maximum momentum transport and maximum total dissipation rate as functions of the Reynolds number. It is also equivalent to minimum Reynolds number as a function of the total stress. The minimum Reynolds number formulation is particularly suited to a wavenumber expansion for the mean and therefore presented here. When discussing this bound we shall often refer to the equivalent maxima.

In this section expressions are derived for the Reynolds number and the boundary condition constraints in terms of the I_k. It is also shown that the stability constraint on the smallest scale relates the stress to k_0, allowing minimization of the Reynolds number as a function of k_0.

First, $\mathrm{d}^2\bar{v}\cdot\boldsymbol{i}/\mathrm{d}z^2 = \mathrm{d}^2U^+(z)/\mathrm{d}z^2$ is expressed using the Fejér series,

$$-\frac{\mathrm{d}^2U^+}{\mathrm{d}z^2} = \sum_0^{k_0}\sum_0^{k_0} I_k I_j \mathrm{e}^{\mathrm{i}(k-j)\phi}. \tag{4.1}$$

Note that the I_k are real for a symmetric profile U^+ (Malkus 1979). Next the boundary conditions on U^+ are determined from (3.1) through the boundary conditions on v and $\overline{uw}$ as

$$\frac{\mathrm{d}^3U^+}{\mathrm{d}z^3} = U^+ = 0, \quad \frac{\mathrm{d}^2U^+}{\mathrm{d}z^2} = R_\tau, \quad \frac{\mathrm{d}U^+}{\mathrm{d}z} = \pm R_\tau \quad \text{at} \quad z = \mp 1. \tag{4.2}$$

The third-derivative conditions are identically satisfied by the Fejér representation while the second-derivative conditions impose a constraint on the I_k. The first-derivative conditions applied to the first integral of the series give a constraint on the I_k^2. The two constraints are

$$\sum_0^{k_0} I_k = R_\tau^{\frac{1}{2}}, \quad \sum_0^{k_0} I_k^2 = R_\tau. \tag{4.3}$$

Finally, an average over the whole domain of the second integral of (4.1) together with the boundary conditions on U^+ leads to

$$R = \tfrac{1}{3}R_\tau^2 - R_\tau \sum_0^{k_0}\sum_0^{k_0}{}_{k\neq j} \frac{I_k I_j}{\pi^2(k-j)^2}. \tag{4.4}$$

In the laminar boundary layer the velocity varies linearly with the distance from the wall, $U^+ = z^+ \equiv R_\tau \delta$. That distance δ_c and velocity U_c which characterize the end of the boundary layer define a critical boundary Reynolds number $R_\mathrm{c} \equiv U_\mathrm{c}\delta_\mathrm{c}/\nu = (z_\mathrm{c}^+)^2$. The Busse–Howard effective boundary-layer thickness $z_\mathrm{c}^+ = 6.3$, determined from the dissipation rate integral, is used as a first approximation. A bound from below for R_c, based on additional constraints, is determined here in §7. Plots of the extremalizing mean profiles show that the boundary layer extends two full wavelengths $\lambda_0 = 2\pi/k_0$ into the flow. That is, $z_\mathrm{c}^+ = 4/k_0$. Rewritten in terms of k_0, the constraint on the smallest scale is

$$k_0 = \frac{4R_\tau}{R_\mathrm{c}^{\frac{1}{2}}}, \tag{4.5}$$

where equality is presumed by absorbing any dependence of R_c on the outer flow into the later determination of R_c. One may now look for the minimum Reynolds number as a function of k_0.

4.2. *The Euler–Lagrange equations*

The Lagrangian for minimum Reynolds number subject to the constraints (4.3), (4.5) is

$$L(k_0) = \tfrac{1}{3}(\tfrac{1}{4}R_\mathrm{c}^{\frac{1}{2}}k_0)^2 - (\tfrac{1}{4}R_\mathrm{c}^{\frac{1}{2}}k_0)\sum_0^{k_0}\sum_0^{k_0}{}_{k\neq j}\frac{I_k I_j}{\pi^2(k-j)^2} + \lambda_1\left(\sum_0^{k_0} I_k - (\tfrac{1}{4}R_\mathrm{c}^{\frac{1}{2}}k_0)^{\frac{1}{2}}\right) + \lambda_2\left(\sum_0^{k_0} I_k^2 - \tfrac{1}{4}R_\mathrm{c}^{\frac{1}{2}}k_0\right), \tag{4.6}$$

where λ_1, λ_2 are Lagrange multipliers. Variation of (4.6) gives the Euler–Lagrange equations,

$$-\tfrac{1}{2}R_c^{\frac{1}{2}} k_0 \sum_{0 \; k \neq j}^{k_0} \frac{I_j}{\pi^2 (k-j)^2} + \lambda_1 + 2\lambda_2 I_k = 0 \tag{4.7}$$

together with (4.3). These are k_0+3 equations for $\{I_k : k = 0, k_0\}, \lambda_1, \lambda_2$.

The degree of this system of algebraic equations can be reduced by a factor of two. First, the solutions respect the symmetry

$$I_k = I_{k_0-k}. \tag{4.8}$$

Second, λ_1 can be eliminated by subtracting pairs of equations. Finally one solves

$$\lambda_2 (I_k - I_{k+1}) - \frac{R_c^{\frac{1}{2}} k_0}{4\pi^2} \left(\sum_{0 \; k \neq j}^{k_0} \frac{I_j}{(k-j)^2} - \sum_{0 \; k+1 \neq j}^{k_0} \frac{I_j}{(k+1-j)^2} \right) = 0 \tag{4.9}$$

together with (4.3) for $\{I_k : k = 0, \lfloor \frac{1}{2}k_0 \rfloor\}$ and λ_2. Here $\lfloor \frac{1}{2}k_0 \rfloor$ means the largest integer smaller than or equal to $\frac{1}{2}k_0$.

The Euler–Lagrange equations for minimum Reynolds number (maximum Nusselt number) are particularly simple because they are linear in the I_k. A difference-equation approximation for large k_0 suggests that the I_k spectrum has the form of a cosine function sufficiently far from the endpoints I_0 and I_{k_0}. Although the exact solution for the spectrum can probably be resolved analytically we choose a numerical representation for comparison with the results for other moments. Optimization of higher moments of the mean leads to nonlinear Euler–Lagrange equations that must be solved numerically. In §4.3 the numerical solution is shown to approach a cosine at high k_0.

4.3. *The optimal solution*

The Euler–Lagrange equations (4.9), (4.3) are solved using Newton's method. The $2\lfloor \frac{1}{2}k_0 \rfloor$ solutions occur in pairs, the I_k spectra of each pair characterized by the number of times a continuous k-like variable ζ is equal to zero. For example, $\zeta = 0$ two times in the spectra corresponding to the two lowest Reynolds numbers and $2\lfloor \frac{1}{2}k_0 \rfloor$ times in the spectra corresponding to the two highest Reynolds numbers (figure 1*a*). The two spectra in each pair are out of phase by roughly π (figure 1*b*).

Figure 2 shows the mean velocity profiles of the twenty solutions for $k_0 = 20$. The area under each curve is proportional to the Reynolds number. The plots span the full channel to emphasize the fact that the entire structure of the mean profile is predicted. The profiles are symmetric about the maximum value, which occurs at the centre of the channel. The conventional logarithmic scale disguises this symmetry.

Of the $2\lfloor \frac{1}{2}k_0 \rfloor$ local minima of (4.9), (4.3), the absolute minimum corresponds to the solution with two zero-crossings and the correct phase. Knowing this, it is not necessary to find all the solutions at higher values of k_0. Mean profiles at four values of k_0 are shown in figure 3 on a traditional constant-stress, semi-log plot. Notice that there is no extended logarithmic region, nor is there a velocity defect law in the interior (figure 4). The arrows on these and subsequent figures indicate the direction of increasing Reynolds number.

The optimal I_k spectrum can be approximated to very high accuracy by a cosine, $I_k = A \cos(B(k - \frac{1}{2}k_0)) + C$, where A, B, C are constant parameters. Two of the parameters are used to satisfy the constraints (4.3) in terms of the third, which is then chosen to minimize the Reynolds number. The error in the Reynolds number at $k_0 = 216$ is 0.13% and decreases with increasing k_0. This simple analytic approximation allows extension of the theory to large values of k_0.

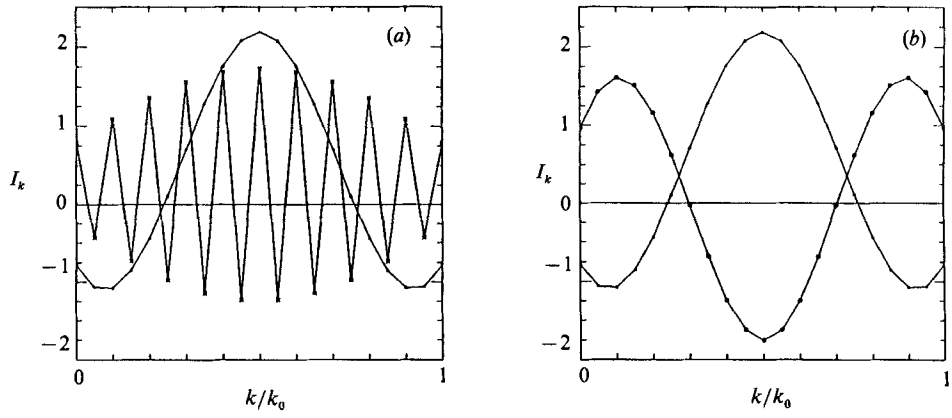

FIGURE 1. (*a*) Spectra of the smallest (·) and largest (×) relative minima of R for $k_0 = 20$. (*b*) Spectra of the two smallest relative minima of R for $k_0 = 20$, labelled · and ·. · marks the absolute minimum.

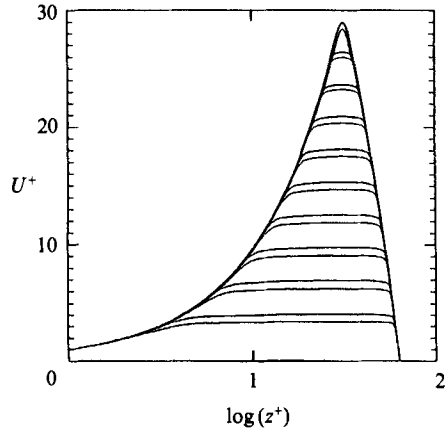

FIGURE 2. The mean profiles of the 20 relative minima of R for $k_0 = 20$.

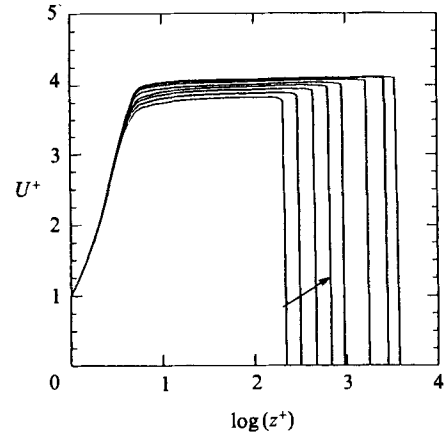

FIGURE 3. Mean profiles for $k_0 = 70$, 100, 150, 216 (numerical) and $k_0 = 300$, 560, 900, 1198 (approximate). Corresponding minima are $R = 412$, 603, 922, 1348; 1893, 3587, 5797, 7742. The arrow indicates the direction of increasing R.

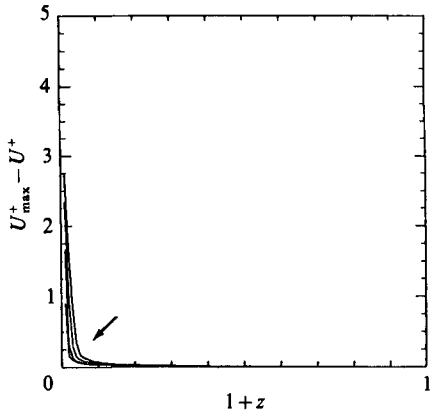

FIGURE 4. The minimum R velocity defect for $k_0 = 70, 100, 150, 216$.

Figure 3 shows the asymptotic behaviour of the high-k_0 profiles. The end of the laminar boundary layer is at $U^+ \approx 4$. A flat interior connects directly to the boundary layer. There is an asymptotically constant value of U^+_{max}, which is less than 2% above the value defining the end of the boundary layer, $U^+ = 4$. The scaled velocity difference, $U^+_{max} - U^+$, is approaching zero in the interior.

In the limit as k_0 approaches infinity,

$$\lim_{R_\tau \to \infty} R \geqslant (4.16 \pm 0.05) R_\tau \quad \text{or} \quad \lim_{R \to \infty} \mathrm{R}_\tau \leqslant (0.240 \pm 0.003) R. \tag{4.10}$$

Busse's nested vortex solution yields

$$\lim_{R_\tau \to \infty} R \geqslant 4.75 R_\tau \quad \text{or} \quad \lim_{R \to \infty} R_\tau \leqslant 0.211 R. \tag{4.11}$$

As anticipated, the upper bound on stress (and consequently on the Nusselt number) is above Busse's because our optimal problem is less constrained. Yet it is clear that this upper-bound problem captures the same gross physics as the more detailed problem addressed by Busse. With this comparison in mind, other bounds are explored in §§5 and 6.

4.4. *Discussion*

A common misconception is illustrated by the optimal mean velocity profiles for maximum Nusselt number. Millikan (1938) argued that Reynolds-number similarity and wall similarity must produce a logarithmic region in the mean velocity. It need not, however, be extensive or with the observed slope. There must be a logarithmic portion of the curves in figure 3 connecting the boundary layer to the interior, but it is vanishingly small. The necessary log region discussed by Millikan is not dynamic in nature. However, the scaled log region of realized turbulent shear flows results from a unique dynamic process.

The maximum Nusselt-number profiles reflect only the boundary physics of observed turbulence. In the interior they are 'flat-topped'. This is because, for fixed Reynolds number, finite shear in the interior decreases the stress. Busse's optimizing vector fields exhibit a constant finite shear which may be due to the approximate nature of the boundary-layer solutions.

5. The mean flows for maximum fluctuation dissipation rate and maximum dissipation rate ratio

5.1. *Assessing bounds by their mean velocity profiles*

Our search for an appropriate optimization principle is among products of the moments related by the dissipation rate integral, equation (2.5). An 'appropriate' principle would be one that captured enough of the essential physics of turbulent flow in channels to give a bound with parametric dependence close to that observed in real flows. The Reynolds-number dependence of any such bound can only be the same as that of the data if the optimal and observed means have similar qualitative structure.

The observed scaled mean velocity, U^+, initially is independent of Reynolds number when plotted against $\log((1+z)R_\tau = \log z^+$. On this constant-stress, semi-log plot there is a laminar boundary layer, an extended linear region (the logarithmic law) and a parabolic interior. The logarithmic sublayer extends further on the plot as the Reynolds number increases but is of constant slope. The interior of the flow is described by the scaled velocity difference, $(U_{\max}-U)/U_\tau$, or the velocity defect. Away from the boundary, the velocity defect is independent of R and is a function of z only. This function of z is referred to as the velocity defect law. The quantitative structure of the observed mean is discussed in §6. (See figure 12.)

Consider the upper bound on the total dissipation rate, $R_\tau^2 R$, presented in §4. The linear dependence of R_τ on R (equation (4.10)) is reflected in the flat-topped structure of the mean profile. One does not expect a $\log R$ dependence as in the data without a scaled, extended logarithmic section in the mean. The optimal profile associated with an 'appropriate' principle should have a velocity defect law as well as a log law. Here and in §6 we use mean profiles to assess the relevance of each bound.

5.2. *The Euler–Lagrange equations*

Here one seeks upper bounds on the fluctuation dissipation rate

$$R_\tau^3\langle\beta\overline{uw}\rangle = R_\tau^2 R - R_\tau^2\langle\beta^2\rangle \tag{5.1}$$

and the dissipation rate ratio

$$I \equiv \frac{R_\tau\langle\beta\overline{uw}\rangle}{\langle\beta^2\rangle} = \frac{R}{\langle\beta^2\rangle} - 1 \tag{5.2}$$

as functions of the Reynolds number. The Euler–Lagrange equations are more difficult than those for maximum total dissipation rate because $\langle\beta^2\rangle$ is a quartic function of the I_k. The Euler–Lagrange equations are therefore cubicly nonlinear in the I_k. It is convenient to fix the Reynolds number and seek the extreme by varying k_0.

In practice the Euler–Lagrange equations are derived for fixed Reynolds number and fixed k_0. Optimization of k_0 is performed after these equations are solved. An advantage of this algorithm is that the Euler–Lagrange equations for maximum $R_\tau^3\langle\beta\overline{uw}\rangle$ and maximum I are the same. For fixed k_0 and fixed Reynolds number, $\langle\beta^2\rangle$ is minimized in each case.

At different values of k_0, the minimum of $\langle\beta^2\rangle$ is found from among the relative minima of the Euler–Lagrange equations. The maxima of $R_\tau^3\langle\beta\overline{uw}\rangle$ and I, as functions of k_0, are thus established. The absolute maxima are found by optimizing k_0. Fortunately, in both cases, the optimal k_0 is a smooth, monotonically increasing function of Reynolds number.

To express $\langle\beta^2\rangle$ in terms of the I_k one integrates (4.1), evaluating the constant of integration using a first-derivative boundary condition of (4.2). Squaring the result and integrating over the whole domain one finds

$$\langle\beta^2\rangle = -\tfrac{1}{3}R_\tau^2 - \frac{R_\tau}{\pi^2}\sum_0^{k_0}\sum_{0\ k\neq j}^{k_0}\frac{I_k I_j}{(k-j)^2} + \frac{1}{\pi^2}\sum_0^{k_0}\sum_0^{k_0}\sum_0^{k_0}\sum_{0\ k\neq j}^{k_0}\frac{I_k I_j I_m I_n}{(k-j)^2}\delta_{k-j,\,n-m}, \tag{5.3}$$

where δ is the Kronecker-delta function.

The Lagrangian for minimum $\langle\beta^2\rangle$ subject to the boundary condition constraints (4.3), the constraint on the smallest scale (4.5) and the Reynolds number given by (4.4) is

$$\begin{aligned} L(R,k_0) = {} & -\tfrac{1}{3}(\tfrac{1}{4}R_{\mathrm{c}}^{\frac{1}{2}}k_0)^2 - \frac{\frac{1}{4}R_{\mathrm{c}}^{\frac{1}{2}}k_0}{\pi^2}\sum_0^{k_0}\sum_{0\ k\neq j}^{k_0}\frac{I_k I_j}{(k-j)^2} \\ & + \frac{1}{\pi^2}\sum_0^{k_0}\sum_0^{k_0}\sum_0^{k_0}\sum_{0\ k\neq j}^{k_0}\frac{I_k I_j I_m I_n}{(k-j)^2}\delta_{k-j,\,n-m} \\ & + \lambda_1\left[\sum_0^{k_0} I_k - (\tfrac{1}{4}R_{\mathrm{c}}^{\frac{1}{2}}k_0)^{\frac{1}{2}}\right] + \lambda_2\left[\sum_0^{k_0} I_k^2 - \tfrac{1}{4}R_{\mathrm{c}}^{\frac{1}{2}}k_0\right] \\ & + \lambda_3\left[R - \tfrac{1}{3}(\tfrac{1}{4}R_{\mathrm{c}}^{\frac{1}{2}}k_0)^2 + \frac{(\frac{1}{4}R_{\mathrm{c}}^{\frac{1}{2}}k_0)}{\pi^2}\sum_0^{k_0}\sum_{0\ k\neq j}^{k_0}\frac{I_k I_j}{(k-j)^2}\right], \end{aligned} \tag{5.4}$$

where λ_1, λ_2, λ_3 are Lagrange multipliers. The associated Euler–Lagrange equations are

$$\frac{(\lambda_3-1)R_{\mathrm{c}}^{\frac{1}{2}}k_0}{2\pi^2}\sum_{0\ k\neq j}^{k_0}\frac{I_j}{(k-j)^2} + \lambda_1 + 2\lambda_2 I_k + \frac{4}{\pi^2}\sum_0^{k_0}\sum_0^{k_0}\sum_{0\ k\neq j}^{k_0}\frac{I_j I_m I_n}{(k-j)^2}\delta_{k-j,\,n-m} = 0 \tag{5.5}$$

together with (4.3), (4.4). These are k_0+4 equations for $\{I_k : k = 0, k_0\}$, λ_1, λ_2 and λ_3. The degree of this system can be reduced by a factor of two in exactly the same manner as described for the minimum-Reynolds-number problem. The symmetry condition (4.8) is again satisfied by all solutions and λ_1 may be eliminated by subtracting pairs of equations. The resultant set of $\lfloor\frac{1}{2}k_0\rfloor+3$ equations for the $\{I_k : k = 0, \lfloor\frac{1}{2}k_0\rfloor\}$, λ_2 and λ_3 is solved using Newton's method.

5.3. *The mean flow for maximum* $R_\tau^3\langle\beta\overline{uw}\rangle$

Using the algorithm described in §5.2 one can find the k_0 and its optimal I_k spectrum that give the maximum $R_\tau^3\langle\beta\overline{uw}\rangle$ for a given Reynolds number. Figure 5 displays the optimal mean profiles for three values of the Reynolds number on a constant-stress, semi-log plot. Although they have more structure than those associated with maximum total dissipation rate, they also lack the ingredients necessary for parametric dependence like that of the data.

From figure 5 one sees that the laminar boundary layer ends at a value of $U^+ \approx 3.5$. The boundary layer gives way to an extended region that is approximately linear but whose slope decreases with increasing Reynolds number. The slope decreases such that the maximum value of U^+ approaches a constant in the asymptotic limit. The asymptotic value of $U^+_{\max}$ is about 25% above the end of the boundary layer, $U^+ \approx 3.5$. Recall that the mean profiles for maximum total dissipation rate also have a maximum value of U^+. However, for maximum total dissipation rate $U^+_{\max}$ is at most 2% above the end of the boundary region.

The scaled mean profile for maximum fluctuation dissipation rate becomes flatter with increasing Reynolds number. Figure 6 shows that the velocity defect for

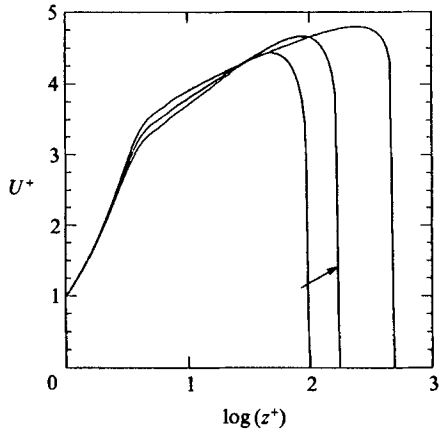

FIGURE 5. Maximum-$R_\tau^3\langle\beta\overline{uw}\rangle$ profiles for $R = 192, 369, 1107$ (corresponding to $k_0 = 31, 55, 154$).

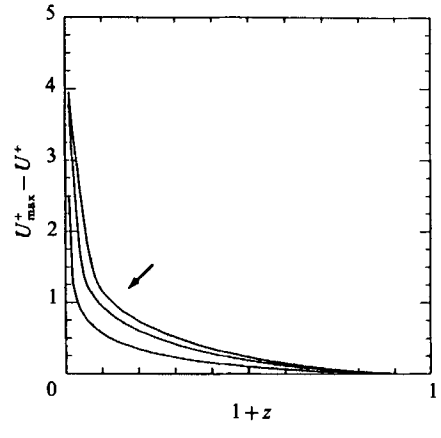

FIGURE 6. Maximum-$R_\tau^3\langle\beta\overline{uw}\rangle$ velocity defect for $R = 192, 369, 1107$.

maximum $R_\tau^3\langle\beta\overline{uw}\rangle$ is approaching zero as R increases. A vanishing velocity defect is associated with a flat curve on the constant-stress, semi-log plot. Maximum fluctuation dissipation rate is similar to maximum total dissipation rate as the Reynolds number approaches infinity.

5.4. *The mean flow for maximum I*

In Ierley & Malkus (1988) a local maximum of the fluctuation dissipation rate ratio, I, is found to be associated with a mean profile 'near' the data. The study is of a two-parameter space that includes the observed mean profile. This discovery suggests an investigation of the global maximum of I.

It was found in §2.3 that an upper bound on I increases as $R^{\frac{1}{2}}$, while in realized flows I increases only as $\log R$. Therefore one does not expect the mean profile for maximum I to be like the observed mean, at least for high R. Rather, a mean profile that diverges from the data can be expected. The mean flow for maximum I is presented for illustration.

To find maximum I as a function of Reynolds number, one again uses the algorithm described in §5.2. Contrary to the profiles for the maxima of the

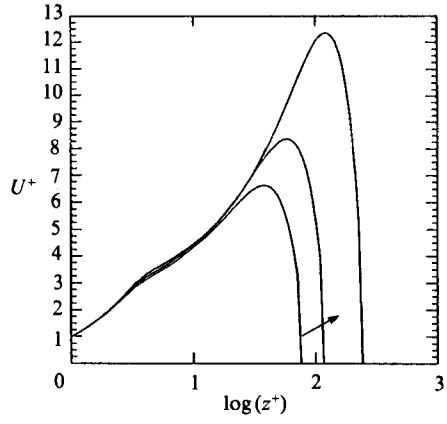

FIGURE 7. Maximum-I profiles for $R = 192, 369, 1107$ ($k_0 = 24, 37, 77$).

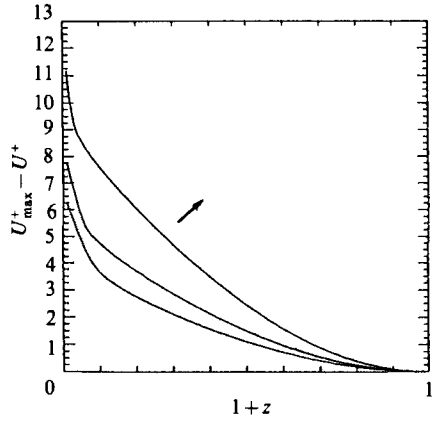

FIGURE 8. Maximum-I velocity defect for $R = 192, 369, 1107$.

dissipation rates, the scaled mean profiles for maximum I become more parabolic with increasing Reynolds number. The constant-stress, semi-log plot (figure 7) shows that the interior is a rapidly growing percentage of the scaled flow. The dominant parabolic interior is characterized by an increasing velocity defect (figure 8). One also sees, in figure 7, that the logarithmic region connecting the interior to the boundary layer is not extended as in the data. The mean flow for the global maximum of I is closer to Poiseuille flow than to turbulent flow.

5.5. *Discussion*

The mean flows for the maxima of $R_\tau^2 R$, $R_\tau^3 \langle \beta \overline{uw} \rangle$ and I are encouraging because they reveal the large variation in internal structure allowed by our formal bounding scheme. None of these bounds, however, leads to a log law or a velocity defect law as seen in the data. These bounds do not capture this important physics of turbulent flow in channels. Clearly, optimization principles 'in between' these extremes should be explored. We therefore consider powers of the scaled stress multiplied by I, that is, quantities of the form $(R_\tau^2/R^2)^n I$. We show in §6 that only the mean flow for $n = 1$ has both a logarithmic law and a velocity defect law.

6. The mean flow for maximum efficiency function $\mathscr{E}$

6.1. *The Euler–Lagrange equations*

Using the dissipation rate integral (3.2), the efficiency function is defined as

$$\mathscr{E} \equiv \frac{R_\tau^2}{R^2} I = \frac{R_\tau^3 \langle \beta \overline{uw} \rangle}{R^2 \langle \beta^2 \rangle} = \frac{R_\tau^2}{R} \left[\frac{1}{\langle \beta^2 \rangle} - \frac{1}{R} \right]. \tag{6.1}$$

Consider the upper bound on $\mathscr{E}$ as a function of Reynolds number. For fixed k_0 and R this problem has already been solved! The solution is that of minimum $\langle \beta^2 \rangle$ given by (5.3) subject to the boundary condition constraints (4.3), the constraint on the smallest scale (4.5) and the expression for R in terms of the I_k, (4.4). In fact this is true for the upper bound on any quantity of the form $(R_\tau^2)^n I$. (Maximizing $\mathscr{E}$ is equivalent to maximizing $R_\tau^2 I$ for fixed Reynolds number.) The Lagrangian is given by (5.4) and the unsimplified form of the Euler–Lagrange equations by (5.5), (4.3) and (4.4). It is only necessary to find the optimal k_0 for maximum $\mathscr{E}$. As was the case for maximum $R_\tau^3 \langle \beta \overline{uw} \rangle$ and maximum I, the optimal k_0 is a smooth, monotonically increasing function of R.

6.2. *The optimal solution*

Maximization of $\mathscr{E}$ as a function of Reynolds number results in the mean flow shown in figure 9. The mean exhibits swift convergence on the constant-stress, semi-log plot. The qualitative internal structure of the asymptotic form resembles that of the data. There is a well-defined logarithmic sublayer and a parabolic interior. The logarithmic layer has constant slope and extends further with increasing Reynolds number. Consistent with the extended log region, the interior has a rapidly converging velocity defect law (figure 10). As will be demonstrated in §6.4, most of the quantitative discrepancy between the maximum-$\mathscr{E}$ mean flow and the data is removed if a larger R_c is used to define the smallest scale. Quantitative assessment of the maximum-$\mathscr{E}$ bound is postponed until then.

6.3. *Asymptotic approximation at high k_0*

The optimal I_k spectrum for maximum $\mathscr{E}$ consists of a smooth interior and a boundary layer at each end. Figure 11 (*a*) shows the spectrum for $k_0 = 128$ which is the optimal k_0 for $R = 1107$. Figure 11 (*b*) is an enlarged plot of the spectral boundary layer near $k = 0$. The boundary layers are analogous to oscillations in a continuous variable. Each boundary layer is a series of jumps away from I_0 or I_{k_0}. The jumps alternate in direction and decrease in magnitude, moving towards the interior. The first jump is seen to be 'positive': $I_0 < I_1$ and $I_{k_0} < I_{k_0-1}$. The relative magnitudes of the jumps approach zero as k_0 increases. For the first two jumps we define $\delta_1 = (I_0 - I_1)/I_0 = (I_{k_0} - I_{k_0-1})/I_{k_0}$ and $\delta_2 = (I_1 - I_2)/I_1 = (I_{k_0-1} - I_{k_0-2})/I_{k_0-1}$. The asymptotic behaviour of the jumps at the ends of the I_k spectrum accounts for the asymptotic behaviour of the logarithmic and interior regions in the mean velocity profile.

An approximation for the I_k spectrum at high k_0 can be constructed using the asymptotic values of $\delta_1 = 0.376$ and $\delta_2 = -0.145$ together with a cosine in the interior, $I_k = A \cos(B(k - \frac{1}{2}k_0)) + C$, for $2 \leqslant k \leqslant k_0 - 2$. Two of the three parameters A, B, C are chosen to satisfy the boundary conditions (4.3) in terms of the third, which is then chosen to maximize $\mathscr{E}$ at a given k_0. The amplitudes I_0 and I_1 are determined from I_2, δ_1 and δ_2. For fixed Reynolds number one must again optimize over k_0.

The approximate mean profiles for $R = 1913$, 2519, 3867 corresponding to $k_0 =$

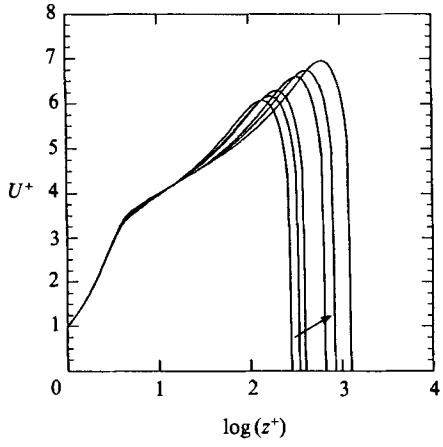

FIGURE 9. Maximum-$\mathscr{E}$ profiles for $R = 738$, 922, 1107 (numerical) and $R = 1913$, 2519, 3867 (approximate). $k_0 = 89$, 109, 128, 210, 270, 400.

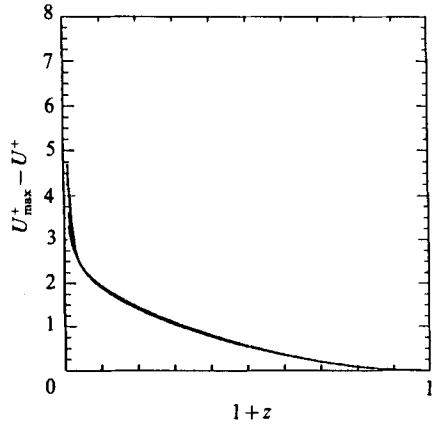

FIGURE 10. Maximum-$\mathscr{E}$ velocity defect law of both the numerical and approximate profiles.

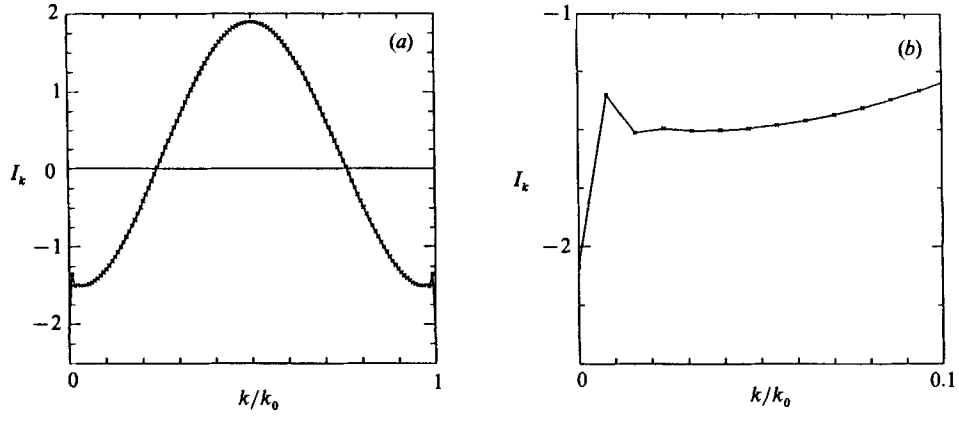

FIGURE 11. (*a*) Maximum-$\mathscr{E}$ spectrum for $R = 1107$. (*b*) Close-up of $\mathscr{E}$-spectrum 'boundary-layer'.

210, 270, 400 were shown in figures 9 and 10 along with the numerical profiles for $R = 738, 922, 1107$ corresponding to $k_0 = 89, 109, 128$. This approximation scheme captures the asymptotic features of the maximum-$\mathscr{E}$ mean profiles. It is therefore used to make quantitative comparisons with the data.

6.4. *Quantitative comparison with the data*

Using the asymptotic approximation to the optimal I_k spectrum described in §6.3, the maximum-$\mathscr{E}$ mean flow can be quantitatively compared to the observed mean flow. Recent channel flow experiments by Johansson & Alfredsson (1983) and Alfredsson & Johansson (1984) determine 5.2 as the slope of the logarithmic region in agreement with earlier data taken by Laufer (1950). Also consistent with Laufer, they find the velocity defect at 0.75 of the half-channel width to be about 5. For Reynolds numbers near 25000 (based on the half-channel width) Johansson & Alfredsson (1983) report 5.0 as the value of the intercept while Laufer finds 5.5. Here we use the more recent data for the constant-stress, semi-log description, with the reservation that a higher value of the intercept was found in the earlier experiments.

As can be seen in figures 9 and 10, the first upper bound on $\mathscr{E}$ predicts a logarithmic slope of 1.26, an intercept of 2.7 and a velocity defect of 1.1 at 0.75 of the half-channel width. It will now be demonstrated that most of the discrepancy can be attributed to the low value of the critical boundary Reynolds number R_c. Recall that the Busse–Howard critical number $R_c = 39.69$, corresponding to a critical boundary scale $z_c^+ = 6.3$, was used as a first approximation. Notice that the beginning of the logarithmic region is at $z^+ \approx 6$ for this R_c.

Figure 12 shows the maximum-$\mathscr{E}$ mean profile calculated using $R_c = 480$ plotted along with the data of Johansson *et al.* (1983), both at Reynolds number approximately 25000. The experimental profile has a more gradual transition from laminar boundary layer to logarithmic sublayer, a higher slope and a larger interior. The logarithmic slope of the maximum $\mathscr{E}$ profile is 4.6 and its intercept is 6.75. The velocity defect at 0.75 of the half-channel width is 4 in the maximum-$\mathscr{E}$ flow and about 5 in the data.

Also shown in figure 12 is the maximum-$\mathscr{E}$ mean for $R_c = 529$ at $R \approx 25000$. Notice that it is entirely above the data, signifying that the corresponding $\mathscr{E}$ is no longer an upper bound. Finally, the maximum-$\mathscr{E}$ profiles for $R_c = 39.69$ and $R_c = 480$ are compared at the same stress (i.e. the same k_0). The upper bounds on $\mathscr{E}$ differ by a factor of about twelve.

6.5. *Adjacent integrals*

What is the result of maximizing $(R_\tau^2)^n I$ for n other than 1? Our calculations suggest that a velocity defect law exists only for $n = 1$. It is seen below that for $n > 1$ the velocity defect decreases as R increases and for $n < 1$ the velocity defect increases as R increases.

The results of maximizing $R_\tau^{\frac{5}{2}} I$ are given in figures 13 and 14. The profiles are like those for maximum $R_\tau^3 \langle \beta \overline{uw} \rangle$ but have more interior at any given Reynolds number. Figure 13 indicates a decreasing logarithmic slope and a constant $U^+_{\max}$ about 30% above the value marking the end of the boundary region (compared to 25% for maximum $R_\tau^3 \langle \beta \overline{uw} \rangle$). Figure 14 shows the decreasing velocity defect. Like the flow for maximum $R_\tau^3 \langle \beta \overline{uw} \rangle$, the maximum-$R_\tau^{\frac{5}{2}} I$ flow is becoming flatter with increasing R.

The mean flow for maximum $R_\tau^{\frac{3}{2}} I$ exhibits the transition between the scaled internal structure of the maximum-$R_\tau^2 I$ flow and the parabolic nature of the maximum-I flow. In figure 15 there appears to be a logarithmic region with a well-

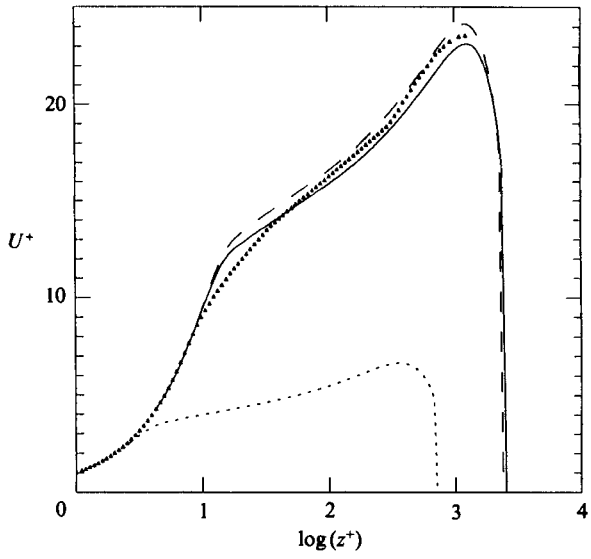

FIGURE 12. Recent experimental data for Poiseuille channel flow, and $\mathscr{E}$ upper-bound profiles for different R_c. △, data (Johansson *et al.* 1983), for $R \approx 25600$; ——, maximum-$\mathscr{E}$ profile with $R_c = 480$ ($k_0 = 230$, $R \approx 25600$); ——, maximum-$\mathscr{E}$ profile with $R_c = 529$ ($k_0 = 210$, $R \approx 25600$); – – –, maximum-$\mathscr{E}$ profile with $R_c = 39.69$ ($k_0 = 230$, $R \approx 2100$).

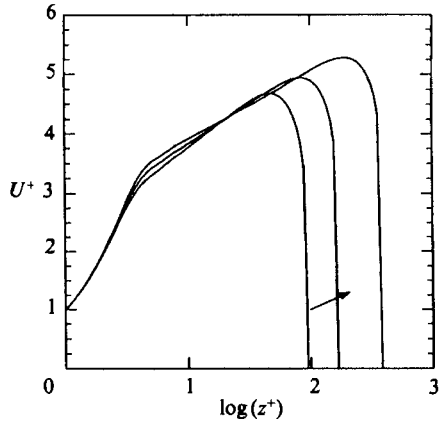

FIGURE 13. Maximum-$R_\tau^{\frac{5}{2}}I$ profiles for $R = 192, 369, 1107$ ($k_0 = 30, 53, 121$).

defined slope. As the Reynolds number increases, however, the logarithmic section does not increase in extent. Rather, the length of the logarithmic layer stays fixed, causing the parabolic interior to dominate U^+ at high Reynolds numbers. Figure 16 shows an increasing velocity defect, indicating again that the scaled flow is becoming more parabolic with increasing Reynolds number.

In terms of the I_k spectra, the boundary structure determines the interior features of the mean velocity profiles. The maximum stress spectra are completely smooth and asymptotically approach a cosine function everywhere. The spectra for maximum $R_\tau^3\langle\beta\overline{uw}\rangle$ are also smooth but diverge from a simple cosine near I_0 and I_{k_0} as R increases.

The class of moments $\{(R_\tau^2)^n I, n \geqslant 0\}$ have spectra with boundary layers. The

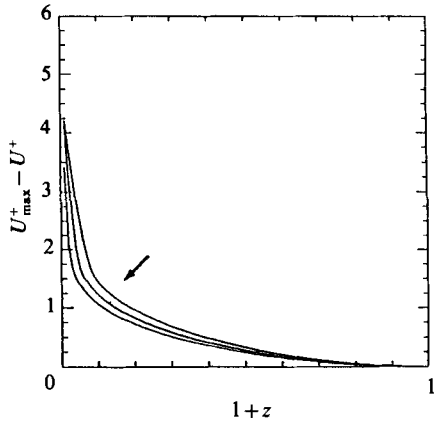

FIGURE 14. Maximum-$R_\tau^{\frac{5}{2}}I$ velocity defect for $R = 192, 369, 1107$.

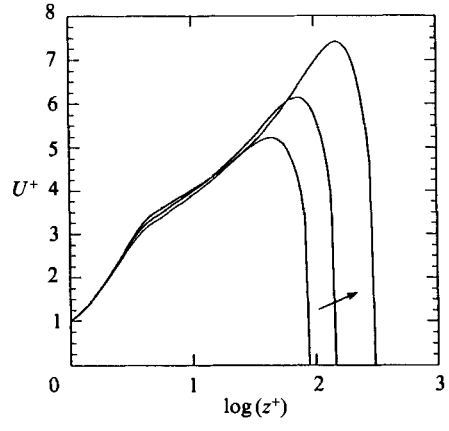

FIGURE 15. Maximum-$R_\tau^{\frac{3}{2}}I$ profiles for $R = 192, 369, 1107$ ($k_0 = 28, 46, 96$).

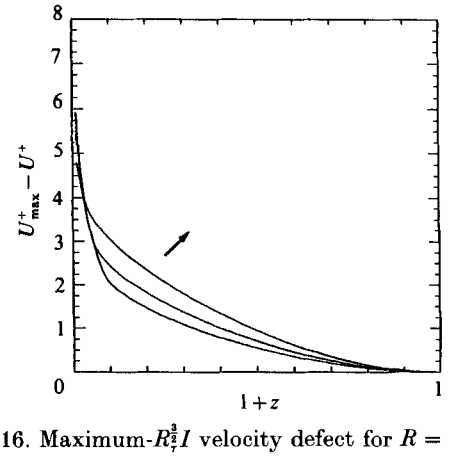

FIGURE 16. Maximum-$R_\tau^{\frac{3}{2}}I$ velocity defect for $R = 192, 369, 1107$.

magnitudes of the jumps characterizing the boundary layers decrease with increasing n. As the jumps decrease in size the interior of the mean also decreases. Figure 17 compares the spectra for the maxima of $R_\tau^3\langle\beta\overline{uw}\rangle$, $R_\tau^{\frac{5}{2}}I$, $R_\tau^2 I$ and $R_\tau^{\frac{3}{2}}I$ at $R = 922$. Only a certain size of the boundary layer in the I_k spectrum leads to scaling as in the data.

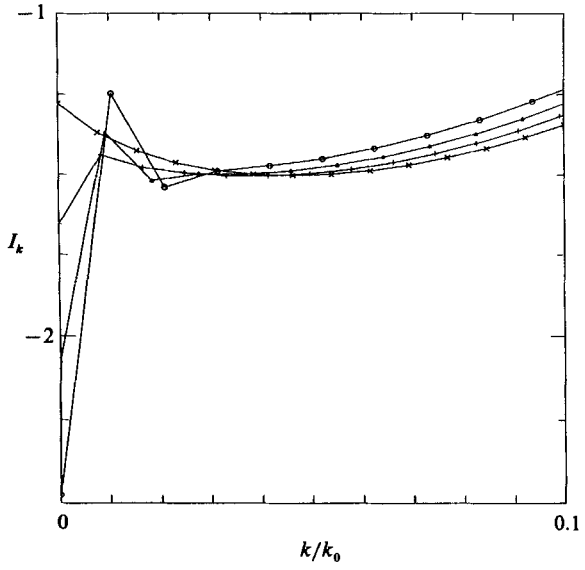

FIGURE 17. Spectra for $R = 922$: ×, maximum $R_\tau^{\frac{2}{3}}\langle\beta\overline{uw}\rangle(k_0 = 130)$; +, maximum $R_\tau^{\frac{1}{3}}I$ $(k_0 = 121)$; △, maximum $\mathscr{E}(k_0 = 109)$; ○, maximum $R_\tau^{\frac{3}{2}}I(k_0 = 96)$.

6.6. *Discussion*

One concludes that the efficiency function $\mathscr{E}$ is unique among functions of the form $(R_\tau^2/R^2)^n I$. Only maximum $\mathscr{E}$ results in an asymptotic velocity defect law. Only with a logarithmic law of a special nature does one find a velocity defect law. The logarithmic region must have a slope independent of Reynolds number. In addition, it must increase in extent with increasing Reynolds number so as to keep the parabolic interior from dominating U^+. Both laws are part of the same inviscid equilibration process which is captured in the maximum-$\mathscr{E}$ mean flow. The extensive logarithmic laws of the data and of the maximum-$\mathscr{E}$ flow are dynamic in nature in contrast to the necessary logarithmic regions discussed by Millikan. Those limited logarithmic regions can be seen linking boundary and interior in all the upper bound mean flows.

Of course there are other quantities that, in the limit of high Reynolds number, are asymptotically similar to $\mathscr{E}$. Examples are $R^{-3}\phi_f I$ and $R^{-3}R_\tau^3 c_f^2$, where $\phi_f = R_\tau^3\langle\beta\overline{uw}\rangle$ and $c_f = (\langle\beta\overline{uw}\rangle/\langle\beta^2\rangle^{\frac{1}{2}})\langle\overline{uw}^2\rangle^{\frac{1}{2}}$. However, each of these alternatives, like $\mathscr{E}$ itself, contain only those low-order moments of the mean that appear in relative stability studies (Malkus & Veronis 1958). This apparent simplicity encourages us to seek a generalizable foundation for statistical stability from global arguments that assess the absolute stability of presumed solutions.

7. Additional constraints on the smallest scale of motion effective in the transport of momentum

7.1. *Recent studies of initial shear flow instability*

The results of §6.4 suggest that the difference between the upper bounds of $\mathscr{E}$ and the observations is largely due to the order of magnitude underestimate of the boundary Reynolds number R_c. The success of the dissipation rate integral as a principal constraint to determine stability criteria for Taylor–Couette flow (Stuart 1958) and

convection (Malkus 1963) is in sharp contrast with the poor estimates of realized stability criteria when it is applied to parallel shear flow (Joseph 1976). It would appear that, not only is the numerical estimate poor, but the dissipation rate integral fails to capture the central physical process at work in the destabilization of parallel flow. Numerical studies at low Reynolds number (Orszag & Patera 1980; Herbert 1983) indicate the importance of a double mechanism, in which stable Orr–Sommerfeld vortex waves initiate local three-dimensional inertial instabilities, which in turn presumably reproduce the waves. Initial features of these inertial instabilities of elliptical vortices have been the subject of many recent papers (Pierrehumbert & Widnall 1982; Pierrehumbert 1986; Bayly 1986; Craik & Criminale 1986; Herbert 1988). The instability is broad-band and grows rapidly, quite suggestive of aspects of the observed 'spots' which initiate shear flow disorder. Also, the spatially local feedback mechanism needed to reproduce the vortex waves has been explored numerically (Henningson, Spalart & Kim 1987). Plausibly, a predictive theoretical framework for the complete symbiotic instability process will soon emerge.

In realized parallel shear flows the Reynolds number at which instability occurs depends upon the amplitude of those small disturbances that exist due to entry conditions or other sources of noise. For normally smooth flow, the observed critical Reynolds number is near 1000. In each of the studies mentioned in the last paragraph an initial or continuing vortex disturbance was assumed. How then can one determine a realistic R_c for the very 'noisy' boundary layer of turbulent flow? In Ierley & Malkus (1988) an approach to this problem was outlined in which one determines an absolute stability criterion for an appropriate Orr–Sommerfeld wave. That method will be discussed and implemented in the last paragraphs of this section.

The more direct approach to the determination of an improved R_c, in the context of upper-bound theory, is the addition of further integral constraints beyond those used by Busse and Howard. Since the vortex wave is a central aspect of realized shear flow, it is plausible that the vorticity dissipation rate integral plays a special role in the small-scale processes in parallel flow, which it does not have in convection or curved flow. Below, these integrals are found and a first step is taken to incorporate their constraints on the optimum vector fields of the smallest scale.

7.2. *Components of the vorticity dissipation rate integral*

From (2.1), the full vorticity equation is written

$$\frac{\partial \boldsymbol{\Omega}'}{\partial t} - \nu \nabla^2 \boldsymbol{\Omega}' + \boldsymbol{v} \cdot \nabla \boldsymbol{\Omega}' - \boldsymbol{\Omega}' \cdot \nabla \boldsymbol{v} = 0, \tag{7.1}$$

where $\boldsymbol{\Omega}' = \nabla \times \boldsymbol{v}$. As in §3, parallel, statistically steady shear flow is considered, with

$$\left.\begin{aligned} \boldsymbol{v} = \boldsymbol{u} + \bar{\boldsymbol{v}}, \quad \boldsymbol{\Omega}' = \boldsymbol{\Omega} + \bar{\boldsymbol{\Omega}}, \\ \bar{\boldsymbol{v}} = U(z)\,\hat{\boldsymbol{\lambda}}, \quad \bar{\boldsymbol{\Omega}} = \nabla \times \bar{\boldsymbol{v}} = \frac{\partial U}{\partial z}(\hat{\boldsymbol{k}} \times \hat{\boldsymbol{\lambda}}), \end{aligned}\right\} \tag{7.2}$$

where as before the overbar is a spatial average in the (x, y)-plane parallel to the boundaries. However, here it is mathematically convenient to choose the mean flow to have the arbitrary direction $\hat{\boldsymbol{\lambda}}$ in the (x, y)-plane. Therefore, without loss of

generality, the integral for the square of the x-component of vorticity, $\boldsymbol{\Omega}\cdot\hat{\boldsymbol{\imath}}\equiv\omega_x$ is written

$$\frac{1}{2}\frac{\partial\langle\omega_x^2\rangle}{\partial t}-\nu\langle\omega_x\nabla^2\omega_x\rangle-\langle\omega_x\boldsymbol{\Omega}\cdot\boldsymbol{\nabla}u_z\rangle-(\hat{\boldsymbol{\jmath}}\cdot\hat{\boldsymbol{\lambda}})\left\langle\omega_x u_x\frac{\partial^2 U}{\partial z^2}\right\rangle-\left\langle\omega_x\frac{\partial U}{\partial z}\frac{\partial}{\partial x}\{\boldsymbol{u}\cdot(\hat{\boldsymbol{k}}\times\hat{\boldsymbol{\lambda}})\}\right\rangle=0. \tag{7.3}$$

The two integrals, (7.3) and the similar equation for the y-component of vorticity, constitute additional constraints for parallel shear flow which may significantly reduce the quantitative error between upper-bound solutions and the observations. However, owing to the cubic nonlinear terms, no general analytical consequences of these constraints have yet been found. Because the optimal solutions of such variational statements usually are smooth in space and time, numerical methods are particularly promising. In this section, a few special features of the vorticity constraint are investigated.

7.3. *Additional constraints on vortex wave flow*

The optimal solutions constrained by the dissipation rate integral alone are streamwise vortices. If, in (7.3), $\hat{\boldsymbol{\imath}}$ is chosen to be the streamwise direction $\hat{\boldsymbol{\lambda}}$, one finds that the cubically nonlinear term and the terms representing interaction with the mean field all vanish for these streamwise solutions. Hence there is no vorticity source in the mean flow to sustain a steady streamwise vortex. However, for more generally directed vortices where $\partial/\partial x=0$ but $\hat{\boldsymbol{\lambda}}\neq\hat{\boldsymbol{\imath}}$, one may write the x-component of vorticity, $\omega_x\equiv\nabla^2\psi$, from (7.1) as

$$\frac{\partial\nabla^2\psi}{\partial t}-\nu\nabla^4\psi+(\boldsymbol{v}\cdot\nabla)\nabla^2\psi-(\hat{\boldsymbol{\jmath}}\cdot\hat{\boldsymbol{\lambda}})\frac{\partial}{\partial y}\left(\frac{\partial^2 U}{\partial z^2}\psi-U\nabla^2\psi\right)=0. \tag{7.4}$$

If this nonlinear form of the Orr–Sommerfeld equation is multiplied by ψ and integrated over the entire flow one obtains

$$\frac{1}{2}\frac{\partial\langle(\boldsymbol{\nabla}\psi)^2\rangle}{\partial t}+\nu\langle(\nabla^2\psi)^2\rangle-(\hat{\boldsymbol{\jmath}}\cdot\hat{\boldsymbol{\lambda}})\left\langle\frac{\partial\psi}{\partial z}\frac{\partial\psi}{\partial y}\frac{\partial U}{\partial z}\right\rangle=0. \tag{7.5}$$

This integral exhibits an aspect of Squire's (1933) theorem, that cross-stream vortices have a maximum source in the mean flow and streamwise vortices none. Orr (1907) and MacCreadie (1931) have used (7.5) to determine a minimum value of Reynolds number which permitted such solutions compatible with the boundary conditions for Poiseuille flow. In those studies it was found that $R_c=87.7$, about twice the value found from the dissipation rate integral. The form of this optimal solution is a cross-stream, 'cat's-eye'-like, vortex wave, of finite phase velocity. Numerical experiments (Orszag & Patera 1980) suggest that the travelling 'local' inflexions which may occur in such a flow do not play a role in further instability.

A sketch of the complete vector field for optimal $\mathscr{E}$, subject to (7.5), is given in figure 18. There, it is presumed that the larger vortices approach the optimal solution permitted by the dissipation rate integral, retaining only the finite-amplitude stability requirements on the mean field inherent in (7.4) (Holm *et al.* 1985). The quantitative value of R_c is still a factor of six too low, corresponding to an underestimate of $\sqrt{6}$ in the scale of the boundary layer and the amplitude of internal features.

Synge (1938) also used a form of (7.5), but his purpose was to estimate properties

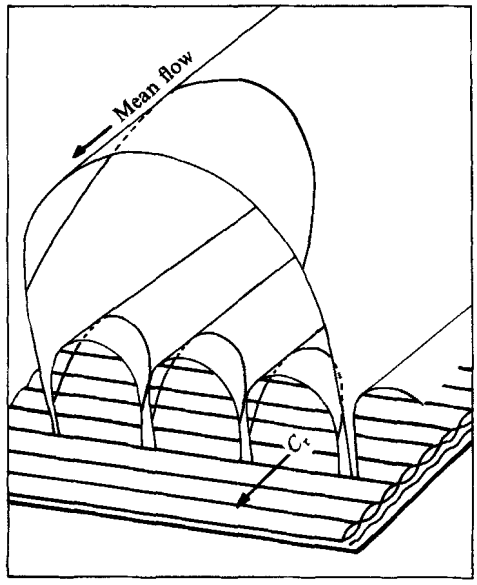

FIGURE 18. Sketch of boundary region of the complete vector field for optimal $\mathscr{E}$, subject to constraint (7.5) on the smallest scale of motion.

of the Orr–Sommerfeld linear eigenvalue problem (Lin 1955; Joseph 1968). If the asymptotic form of the Orr–Sommerfeld wave is used in (7.5) to estimate an R_c, the result is quite close to the experimental value (Malkus 1956). A similar, but entirely numerical, result is reported in Ierley & Malkus (1988). It is clear from that work and the reformulation here that (7.5) is not really a vorticity constraint, but a component of the energy dissipation rate integral whose isolation is permitted by the assumption that the optimal solutions have the form of vortex waves. However, if (7.4) is multiplied by $\nabla^2\psi$ and integrated, the vorticity dissipation rate integral (7.3) for axisymmetric vector fields is recaptured. Recalling that $\boldsymbol{\lambda}$ defines the (arbitrary) streamwise direction in the (x, y)-plane, use of the horizontal average of the basic equation (2.1) establishes that

$$-(\hat{\boldsymbol{j}}\cdot\hat{\boldsymbol{\lambda}})\left\langle \omega_x u_z \frac{\partial^2 U}{\partial z^2}\right\rangle = \frac{1}{\nu}\langle(\omega_x u_z)^2\rangle. \tag{7.6}$$

Hence, (7.3) for axisymmetric flow can be written

$$\nu\nabla^2\psi\frac{\partial\nabla^2\psi}{\partial z}\bigg|_{\mathrm{B}} = \nu\langle\{\boldsymbol{\nabla}(\nabla^2\psi)\}^2\rangle + \frac{1}{\nu}\langle(u_z\nabla^2\psi)^2\rangle, \tag{7.7}$$

where the boundary terms, $|_{\mathrm{B}}$, on the left are the vorticity source. A minimum critical Reynolds number for a vector field satisfying previous constraints plus (7.7) has not yet been determined.

These several restrictions on two-dimensional solutions may suggest why parallel shear flows have such delayed and complex instabilities. Certainly the first three-dimensional vector fields compatible with the full vorticity dissipation rate (7.3) will assist in understanding the underlying order of the realized complex flow.

7.4. *Absolute stability of Orr–Sommerfeld waves*

Numerical studies of the secondary instability of Orr–Sommerfeld vortex waves (Herbert 1983; Orszag & Patera 1983; Zaff 1987; Ierley & Malkus 1988) lead to the

conclusion that the cross-stream spatial scale of the growing inertial disturbances are as large and larger than the cross-stream scale of the finite-amplitude Orr–Sommerfeld wave. Hence, the Reynolds-number dependence of the smallest scale of motion ($k_0(R)$ in (4.5)) contributing to the transfer of momentum can be estimated from below by determining a critical boundary Reynolds number for stability of a vortex wave of primary cross-stream scale k_0 and arbitrary amplitude. A modified use of the dissipation rate integral as principal constraint permits the determination of a maximum value for this minimum Reynolds number, assuring stability for any vortex amplitude (in §7 of Ierley & Malkus 1988). In brief, the usual absolute stability function (Joseph 1976) is rewritten with an additional constraint as

$$R_{\text{abs}} = \min_v \frac{\langle \boldsymbol{v} \cdot \nabla^2 \boldsymbol{v} + \boldsymbol{v} \cdot \nabla \phi + \lambda_2(z)(\overline{uw} - \overline{u'w'}) \rangle}{\langle \boldsymbol{v} \cdot \boldsymbol{v} \cdot \nabla U \rangle}, \tag{7.8}$$

where, for the mean profile U, $\overline{u'w'}(z)$ is the normalized Reynolds stress of the marginal Orr–Sommerfeld wave, ϕ is the effective pressure and the Lagrange multiplier $\lambda_2(z)$ is chosen so that the Reynolds stress of the eigenfunction $\boldsymbol{v}$ is of identical form to that of the vortex wave. An approximate numerical procedure is used to determine R_{abs} of (7.8), and is reported graphically in figure 9 of Ierley & Malkus (1988). Since the Orr–Sommerfeld waves near the boundary overlap into the adjacent logarithmic layer, it is found that R_{abs} is (weakly) dependent on the logarithmic slope of U. However, for slopes between one-half and twice the observed slope it is found in Ierley & Malkus (1988) that $R_{\text{abs}} = 453 \pm 25$. Hence in a turbulent boundary layer, buffeted by disturbances of all sizes, an estimate from below of the R_c in (4.5) is R_{abs}. The sketch of the optimum vector field remains the same as that pictured in figure 18. However, the boundary vortex is now seen as an Orr–Sommerfeld wave on the verge of three dimensional instability.

8. Upper-bound solutions as mean fields

8.1. *Limitations of the upper-bound models*

The previous section points a way to both qualitative and quantitative improvement of an upper-bound model of turbulent Poiseuille flow. A universal determination of which upper bound, if any, best emulates the realized statistical stability conditions has not been achieved. The function $\mathscr{E}$ of §6 may prove to have unique properties only for channel flow. Exploration of its generality based on relative stability arguments is in progress.

With sufficient additional integral constraints, the vector fields optimizing $\mathscr{E}$ will have many statistical properties very close to the observations. Is such a smooth mechanistic model a satisfactory picture of turbulence? – hardly! Turbulence implies disorder and non-periodic behaviour. Momentum transporting elements in realized shear flow are highly intermittent. The typical correlation of transporting fields is near 50%. Order and disorder strike a delicate balance in turbulent flow. In this section several paths are suggested for using the upper-bound vector fields as new starting points for studies of time dependence in turbulence.

8.2. *Intermittency near the extreme fields*

The Euler–Lagrange equations (3.5) for upper-bound solutions have linear terms identical in form to those of the Navier–Stokes equations, (2.1). Also both sets of equations have identical first integrals relating mean gradients and mean momentum

transport, e.g. (3.1). Hence, the Navier–Stokes fluctuation equations for statistically steady turbulent shear flow may be rewritten symbolically as

$$\frac{\partial \boldsymbol{u}}{\partial t} + \nabla p - \nu \nabla^2 \boldsymbol{u} + G = G - (\boldsymbol{u} \cdot \nabla \bar{\boldsymbol{v}} + \bar{\boldsymbol{v}} \cdot \nabla \boldsymbol{u} + \boldsymbol{u} \cdot \nabla \boldsymbol{u}), \tag{8.1}$$

where G represents the nonlinear terms of the Euler–Lagrange equation and the overbars indicate a horizontal average. Although the right-hand side of (8.1) is zero-average, the instantaneous value can be order one due to the observed intermittency of the flow. However, if the upper-bound solutions found when the right-hand side of (8.1) is set equal to zero are quantitatively realistic, then the presumption can be made that the net effect of the right-hand terms is small. This permits a formal study of departures from the amplitude balance achieved by the α_m modes of the extreme vector field. Such a codimension-m bifurcation problem plausibly is quite non-periodic. Bergé, Pomeau & Vidal (1987) assures us that if $m = 3$ or greater the characteristic finite-amplitude equilibration is through intermittent behaviour. Turbulent shear flow certainly is not a low-order dynamic system, but the extreme vector fields of the upper-bound theory can be treated as a finite-order dynamic system. Since one could explore the temporal interaction of a subset of the α_m smooth fields (e.g. the five largest modes), numerical study seems quite promising. Decorrelation of the fields found in such a study could improve the deductive consequences of the upper-bound model. This address to the time-dependent dynamics of the large-scale flow might be formulated as a quantitative alternative to the continuing search for 'sub-grid scale' numerical algorithms.

8.3. *Closure near the extreme field*

The form of the right-hand side of (8.1) suggests that closure approximations, particularly the 'direct-interaction approximation' (DIA) of Kraichnan (1955, 1959) might be employed to decorrelate the upper-bound extreme fields. A study by Herring (1964) is particularly relevant. Herring considered thermal convection at infinite Prandtl number, numerically solving first the mean field problem for steady cellular convection, and then applying DIA as a second step. He found that the decorrelations led to a 10% reduction of the heat flux from that due to the steady cells. Chan (1971) also studied this problem, but sought an upper bound. He established that the maximum heat flux was identical to the mean field heat flux at large Rayleigh number, both differing from the observations by a factor of approximately two. Hence, either the mean field problem or the Euler–Lagrange problem for maximum heat flux can be used in an extension to high Rayleigh numbers of Herring's application of DIA.

Unfortunately, solutions for the one-dimensional mean field problem for turbulent Poiseuille flow are far from the observed flow (Ierley & Malkus 1988). Three-dimensional instabilities on complicated two-dimensional wavy structures appear to dominate the equilibration of that flow. However, here solutions of a Euler–Lagrange equation such as (3.5) could serve as the 'mean' field in a study of the decorrelations resulting from a DIA-like closure.

8.4. *Towards order from the side of disorder*

A recent paper by Yakhot & Orszag (1986) estimates several shear flow properties with an ingenious use of a modified DIA and renormalization theory. Although DIA is oriented towards explanation of isotropic homogeneous disorder in a spectral domain, one can think of it as a quantitative stirring mechanism capable of

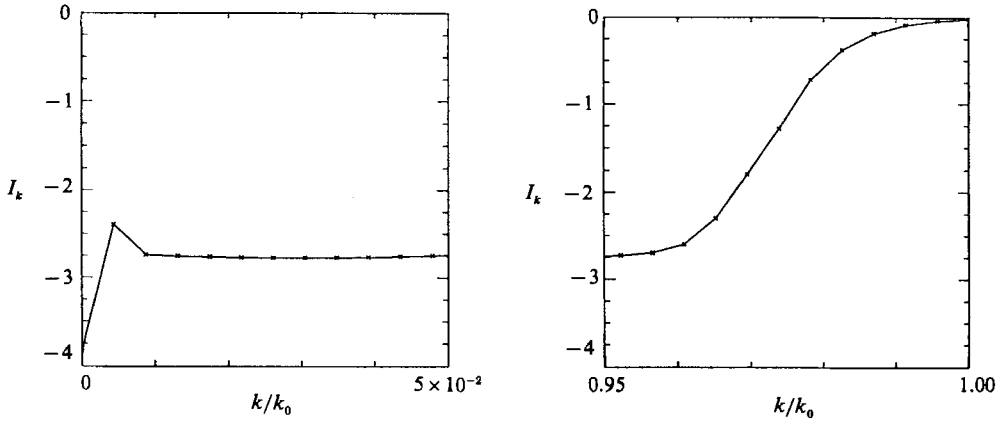

FIGURE 19. A 'realistic' I_k spectrum, with the optimal Gibbs-like spikes removed at high k and with abrupt truncation replaced by an exponential tail.

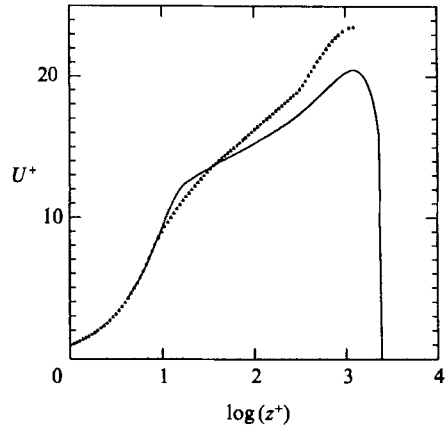

FIGURE 20. The mean velocity profile deduced from the I_k spectrum of figure 19 superimposed on the Alfredsson & Johansson (1984) data (▲).

enhancing local transport along a prescribed gradient of a fluid property. The example given in Yakhot & Orszag is momentum transport along a prescribed logarithmic mean velocity profile, whose amplitude is related to that transport. Their theory and its results do not bear upon the boundary region, the interior region, or the extent of the presumed logarithmic layer, but predict a slope for that logarithmic layer (the von Kármán constant) close to the observations. Whether this speaks well for the presumed amplitude–transport relation, the modified DIA, or both acting together is yet to be determined. However, their methods could be applied to the right-hand terms in (8.1) to produce a modified statistical picture, estimating disordered aspects of an ordered upper-bound flow.

8.5. *Anticipated changes in the extreme I_k spectra*

The modifications of the upper-bound solutions partially implemented in §7 and discussed in §§8.3, 8.4 above presumably will smooth abrupt space–time features of the extreme spectra. For example, it is unlikely that a sharp high-wavenumber cutoff or the nearby Gibbs-like feature of the I_k extreme spectrum, figure 11

would survive. It is also plausible that the critical boundary Reynolds number would increase. To anticipate the consequence of such 'rounding', the tail of the extreme spectrum was arbitrarily modified as shown in figure 19. The Gibbs features are removed and the tail is a smooth exponential function of k. The resulting velocity profile is shown in figure 20 with the $R_c = 453$ from §7, and compared with the data, figure 16. There appears to be little qualitative change in the velocity field, and such change as there is might move the profile nearer to the observations if the R_c also were increased. This insensitivity to significant distortion of the extreme spectrum suggests that $\mathscr{E}$ is a robust statistical stability criterion for channel flow.

Both authors received support for this study under grant ATM86-11727 of the National Science Foundation, for which we are most grateful. The computations were performed on the MIT Mathematics Department's Sun system.

REFERENCES

ALFREDSSON, P. H. & JOHANSSON, A. V. 1984 On the detection of turbulence-generating events. *J. Fluid Mech.* **139**, 325.

ARNOL'D, V. I. 1965 Conditions for non-linear stability of the plane stationary curvilinear flow of an ideal fluid. *Dokl. Akad. Nauk SSSR* **162**, 975.

BAYLY, B. 1986 Three dimensional instability of elliptic flow. *Phys. Rev. Lett.* **57**, 2160.

BAYLY, B., ORSZAG, S. & HERBERT, T. 1988 Instability mechanisms in shear-flow transition. *Ann. Rev. Fluid Mech.* **20**, 359.

BERGÉ, P., POMEAU, Y. & VIDAL, C. 1987 *Order within Chaos*, Chapter IX. Wiley.

BUSSE, F. 1969 Bounds on the transport of mass and momentum by turbulent flow. *Z. Angew. Math. Phys.* **20**, 1.

BUSSE, F. 1970 Bounds for turbulent shear flow. *J. Fluid Mech.* **41**, 219.

BUSSE, F. 1978 The optimum theory of turbulence. *Adv. Appl. Mech.* **18**, 77.

CHAN, S. K. 1971 Infinite Prandtl number turbulent convection. *Stud. Appl. Maths* **50**, 13.

CRAIK, A. D. D. & CRIMINALE, W. O. 1986 Evolution of wavelike disturbances in shear flows: a class of exact solutions of the Navier–Stokes equations. *Proc. R. Soc. Lond.* **406**, 13.

HENNINGSON, D. S., SPALART, P. & KIM, J. 1987 Numerical simulation of turbulent spots in plane Poiseuille and boundary-layer flows. *Phys. Fluids* **30**, 2914.

HERBERT, T. 1983 Secondary instability of plane channel flows to subharmonic three-dimensional disturbances. *Phys. Fluids* **26**, 871.

HERBERT, T. 1988 Secondary instability of boundary layers. *Ann. Rev. Fluid Mech.* **20**, 487.

HERRING, J. 1964 Investigation of problems in thermal convection. *J. Atmos. Sci.* **21**, 277.

HOLM, D. D., MARSDEN, J., RATIN, T. & WEINSTEIN, A. 1985 Nonlinear stability of fluid and plasma equilibria. *Phys. Rep.* **123**, 1.

HOWARD, L. N. 1963 Heat transport by turbulent convection. *J. Fluid Mech.* **17**, 405.

HOWARD, L. N. 1972 Bounds on flow quantities. *Ann. Rev. Fluid Mech.* **4**, 473.

IERLEY, G. R. & MALKUS, W. V. R. 1988 Stability bounds on turbulent Poiseuille flow. *J. Fluid Mech.* **187**, 435.

JOHANSSON, A. V. & ALFREDSSON, P. H. 1983 Measurements of wall-bounded turbulent shear flows. *J. Fluid Mech.* **137**, 408.

JOSEPH, D. D. 1968 Eigenvalue bounds for the Orr–Sommerfeld equation. *J. Fluid Mech.* **33**, 617.

JOSEPH, D. D. 1976 *Stability of Fluid Motions*, vols. 1 and 2. Springer.

KRAICHNAN, R. 1955 Direct-interaction approximation for isotropic homogeneous turbulence. *Phys. Rev.* **55**, 18.

KRAICHNAN, R. H. 1959 The structure of isotropic turbulence at very high Reynolds numbers. *J. Fluid Mech.* **5**, 497.

KROMMES, J. A. & SMITH, R. A. 1987 Rigorous upper bounds for transport due to passive advection by inhomogeneous turbulence. *Annls Phys.* **177**, 246.

LIN, C. C. 1955 *The Theory of Hydrodynamic Stability.* Cambridge University Press.

MACCREADIE, W. T. 1931 On the stability of the motion of a viscous fluid. *Proc. Natl Acad. Sci. USA* **17**, 381.

MALKUS, W. V. R. 1956 Outline of a theory of turbulent shear flow. *J. Fluid Mech.* **1**, 521.

MALKUS, W. V. R. 1963 Outline of a theory of turbulent convection. In *Theory and Fundamental Research in Heat Transfer*, p. 203. Pergamon.

MALKUS, W. V. R. 1979 Turbulent velocity profiles from stability criteria. *J. Fluid Mech.* **90**, 401.

MALKUS, W. V. R. & VERONIS, G. 1958 Finite amplitude cellular convection. *J. Fluid Mech.* **4**, 225.

MILLIKAN, C. B. 1938 A critical discussion of turbulent flow in channels and circular tubes. *Proc. 5th Intl Congr. Appl. Mech., Cambridge, Ma.*, p. 386.

ORR, W. M. F. 1907 The stability or instability of the steady motions of a perfect liquid and of a viscous liquid. *Proc. R. Irish Acad.* **27**, 9 and 69.

ORSZAG, S. & PATERA, P. T. 1980 Subcritical transition to turbulence in plane channel flows. *Phys. Rev. Lett.* **45**, 989.

ORSZAG, S. & PATERA, P. T. 1983 Secondary instability of wall-bounded shear flows. *J. Fluid Mech.* **128**, 347.

PIERREHUMBERT, R. 1986 Universal short-wave instability of two-dimensional eddies in an inviscid fluid. *Phys. Rev. Lett.* **57**, 2157.

PIERREHUMBERT, R. & WIDNALL, S. 1982 Two- and three-dimensional instabilities of a spatially periodic shear layer. *J. Fluid Mech.* **114**, 59.

SQUIRE, H. B. 1933 On the stability of three-dimensional disturbances. *Proc. R. Soc. Lond.* A **132**, 621.

STUART, J. T. 1958 On the non-linear mechanics of hydrodynamic stability. *J. Fluid Mech.* **4**, 1.

SYNGE, J. 1938 Hydrodynamical stability. *Semicent. Publ. Amer. Math. Soc.*, vol. **2**, p. 227.

YAKHOT, V. & ORSZAG, S. A. 1986 Renormalization-group approach to turbulence. *J. Sci. Comput.* **1**, 3.

ZAFF, D. 1987 Secondary instabilities in Ekman boundary flow. Ph.D. thesis, Dept. of Maths, MIT.